Measurements of the energy dissipation rate in homogeneous turbulence using dense 3D Lagrangian Particle Tracking and FlowFit

A. Schröder[1,2], D. Schanz[1], S. Gesemann[1],
F. Huhn[1], T. Buchwald[2], D. Garaboa Paz[3] and E. Bodenschatz[4]
1: German Aerospace Center (DLR), Institute of Aerodynamics and Flow Technology, Göttingen, Germany
2: Brandenburgisch Technische Universität (BTU) Cottbus-Senftenberg, Germany
3: Group of Non-linear Physics, University of Santiago de Compostela, Spain
4: Laboratory for Fluid Dynamics, Pattern Formation and Biocomplexity,
Max-Planck-Institute for Dynamics and Self-Organization, Göttingen, Germany
* Correspondent author: andreas.schroederl@dlr.de

Keywords: 3D LPT, Velocity Gradient Tensor, turbulent energy dissipation rate, Shake-The-Box, FlowFit

ABSTRACT

We present measurements of the full velocity gradient tensor and all volumetric dissipation rate elements based on dense fields of fluid particle trajectories in homogeneous turbulence at Re_λ ~270 and ~370 in a Kármán flow between two counter-rotating disks with impellers. Applying the Shake-The-Box (STB) Lagrangian Particle Tracking (LPT) algorithm, we are able to instantaneously track up to 80.000 particles in a volume of 40 x 40 x 15 mm^3. The mean inter-particle distance is lower than 7 Kolmogorov lengths for the Re_λ ~270 case. A data assimilation scheme (FlowFit) with continuity and Navier-Stokes- constraints is used to interpolate the scattered velocity and acceleration data by a continuous 3D B-Spline representation, enabling to recover (locally) the smallest flow scales. In the presentation, we show Lagrangian velocity and acceleration statistics, as well as the Eulerian counterparts on velocity gradients and pressure fields. We compute the energy dissipation rate directly by making use of quadruples of particle trajectories in close proximity ($r < 3\eta$) and compare it to indirect approaches using second-order velocity- and velocity-acceleration structure functions in the inertial subrange.

1. Introduction

The Richardson-Kolmogorov cascade model states that after transition from laminar to turbulent states of fluid motion the flow in wind tunnels, pipes, jets, wakes or along plates and moving surfaces is injecting kinetic energy into the turbulence at large scales which break down to smaller and smaller scales due to entrainment effects, shear instability mechanisms and the dynamics of turbulent scale interaction. Thereby, a picture of turbulence has been created that intrinsically connects this (in general) directional down-scaling process, featuring the development and decay of vortical flow structures (or enstrophy ω^2) with the overall energy transfer, finally ending into viscous dissipation and heat at the smallest scales of the cascade. The energy transfer mechanism over many scales of turbulent structures is governed by the (local) energy dissipation rate ε and plays a significant role for the understanding of turbulence and its self-sustaining spatial and temporal organization. It delivers the knowledge about the rate of energy transferred globally

from scale-to-scale and locally into heat in an instantaneous and statistical sense in turbulent motion. After Pope (2000) the picture of the cascade indicates that ε at sufficiently high Reynolds numbers has to scale with ~U^3/L, with U^2 representing the turbulent kinetic energy and L the integral length scale of the turbulent motion. If the range of spatial scales found in the turbulent structures is large enough, while the range is increasing with Reynolds number approximately with $L/\eta \sim Re_L^{9/4}$ (Vassilicos 2015) or $L/\eta = Re_\lambda^{3/4}$ and $T_L/\tau_\eta = Re_\lambda^{1/2}$ (Toschi and Bodenschatz 2009) with λ being the Taylor microscale, η being the Kolmogorov length scale and corresponding time scales T_L and τ_η, a third range of scales develops, where neither the peculiarities of energy injection (at scales ~L), nor viscous dissipation at small scales ~η influence the spatial scale-to-scale energy transfer, which is called inertial (sub-)range. In this intermediate range, following a -5/3 power law in the corresponding wavenumber spectrum, statistical properties can be described by a balance of the scale-to-scale transfer of kinetic energy and the kinetic energy dissipation rate ε (dissipated power per unit mass). These unique statistical properties in the inertial subrange are used by several methods allowing to approximate ε without the need of resolving the full (fluctuating) velocity gradient tensor A_{ij} at the smallest scales. In the inertial subrange of the cascade of flow structures estimates of ε can be calculated using the energy spectra e.g. via two-point correlation functions or by second- or third order structure functions (the latter known from the famous -4/5's-law (Kolmogorov 1941)) e.g. of the longitudinal component (see e.g. Mann et al 1999 or Xu and Chen 2012) or by the velocity-acceleration structure function $-2\varepsilon = \langle \delta u \cdot \delta a \rangle$ (Falkovich et al. 2012), while all methods assume at least homogeneity. However, it has been shown that for many turbulent flows significant anisotropy remains for the velocity and acceleration vector fields and respective two-point statistics at the inertial subrange (Davidson 2004) or even down to dissipative scales even at higher Reynolds numbers. Furthermore, large kinetic energy dissipation and acceleration events happen intermittently in time and space and are depending on specific interactions of large(r) energy containing flow structures involving the non-local pressure Hessian (Hamlington et al. 2008, Elsinga et al. 2017). The respective PDFs are deviating from Gaussian distributions at high values and therefore, the reasons for the known statistical properties of the inter-scale energy transfer are still not fully understood.

Therefore, a method for a direct 3D measurement of the full A_{ij} resolving all relevant scales at once is still required, which would allow to statistically estimate all energy dissipation rate terms of ε without assumptions of symmetry, homogeneity or (local) isotropy. According to Kolmogorov's similarity hypothesis the turbulence statistics of the velocity gradients at dissipative scales are governed only by the kinematic viscosity ν and the energy dissipation rate ε:

$$\varepsilon = 2\nu\overline{S_{ij}S_{ij}} = \nu\overline{\left(\frac{\partial u_i}{\partial x_j} + \frac{\partial u_j}{\partial x_i}\right)\frac{\partial u_j}{\partial x_i}} =$$

$$\overline{\nu(2\left(\frac{\partial u_x}{\partial x}\right)^2 + 2\left(\frac{\partial u_y}{\partial y}\right)^2 + 2\left(\frac{\partial u_z}{\partial z}\right)^2 + \left(\frac{\partial u_x}{\partial z}\right)^2 + 2\frac{\partial u_x}{\partial z}\frac{\partial u_z}{\partial x} + \left(\frac{\partial u_z}{\partial x}\right)^2 + \left(\frac{\partial u_y}{\partial x}\right)^2 + 2\frac{\partial u_y}{\partial x}\frac{\partial u_x}{\partial y} + \left(\frac{\partial u_x}{\partial y}\right)^2 + \left(\frac{\partial u_z}{\partial y}\right)^2 + 2\frac{\partial u_z}{\partial y}\frac{\partial u_y}{\partial z} + \left(\frac{\partial u_y}{\partial z}\right)^2)}$$

The 12 terms of the dissipation rate equation consist of three squared terms in which the gradient of each velocity component has to be determined along the same direction, six squared terms in which the gradient of each velocity component has to be determined along the other two directions respectively and three further mixed terms. Without the temporal or ensemble average the equation expresses the instantaneous local scalar value for ε. Evaluating the equation requires the accurate (non-intrusive) measurement of all three velocity components and their gradients in all directions at the same location and instant at a resolution close to (or even below) η. These challenging requirements cannot be fulfilled easily and have been tackled experimentally in the past using a step-by-step approach depending on the status of the available techniques. Measurement techniques with specific hardware properties like hot-wire probe methods are restricted to single-points in space and necessitate estimating ε by applying Taylor's frozen turbulence hypothesis with restrictive isotropy and homogeneity assumptions. Hot-wires produce effects of intrusiveness especially when operating in close proximity to walls or to a second (or even further) hot-wire probe(s), in case velocity differences are measured directly. Non-intrusive optical methods like 2D PIV (Raffel et al. 2018, Saarenrinne and Piirto 2000, Xu and Chen 2013) need to assume conditions of symmetry and homogeneity, while Tomo PIV results (Tokgoz et al 2012, Lawson and Dawson 2015), even at high magnification factors or low Reynolds numbers with relatively large values of η, struggle with the low-pass filtering effects of correlation windows when estimating the required instantaneous velocity gradients. Additionally, measurement noise caused by the presence of ghost particles and by the peak detection method of local correlation maps is amplified when calculating derivative values with central difference schemes (or else) on 2D- or 3D velocity vector grids.

On the other side, classical 3D PTV/LPT techniques have been used in turbulence research since decades (e.g. LaPorta et al. 2001), but do not allow resolving the full velocity gradient tensor (VGT) (nor the related pressure fields) due to limitations of the respective evaluation algorithms in reconstructing a sufficient amount of 3D particle trajectories in dense spatial proximity in sufficiently sized measurement volumes. The related image processing methods are typically restricted to low particle image densities (max. up to 0.005 particles per pixel, Malik et al. 1993,

Ouellette et al. 2006). This in turn massively reduces the likelihood finding tetrahedrons of particle trajectories (Xu et al. 2011) running across each other in close proximity of less than ~2η radius, which would allow to resolve most of the local velocity gradients in all directions with central difference schemes directly. But even this approach is still struggling with the amplification of the high particle position error when calculating velocity gradients, especially for close proximity particle constellations and thus eventually overlapping particle images. The first work presenting a (moderately accurate) direct estimation of the (low-pass filtered) VGT in low Reynolds number homogenous turbulence was done by Lüthi et al 2005 using classical 3D-PTV data with linear interpolation between tetrahedrons of particles in closer proximity, thus no velocity gradient curvature effect could be considered.

Due to the severe problems associated with the classical measurement techniques described above in estimating all terms of the dissipation rate ε equation because of low pass filtering, (systematic) noise and/or intrusiveness issues when aiming at resolving the smallest scales of the velocity gradients at sufficiently high Reynolds numbers, there have been only few reports on experimental investigations aiming at a direct determination of all terms of ε , mostly with relatively large error bars and uncertainties. Therefore, PIV related measurements of velocity gradients typically can only claim resolving the full inertial range, sometimes down to the larger dissipative scales, but need to rely on proper correction schemes reflecting the various error sources (Tanaka and Eaton 2007) when the smallest scales are considered. A more recent study in a von Kármán flow (Knutsen et al. 2019) used scanning PIV with a two-camera MART processing for volumetric reconstruction in order to achieve the full local 3D velocity gradient tensor A_{ij} (slightly low pass-filtered with cubic 3D correlation-window sizes of ~3η in each direction). They investigated anisotropy and directionality effects of the inter-scale energy transfer based on the generalized version of the Kármán-Horwarth equation, extended by Monin and Hill.

Recent developments in dense Lagrangian Particle Tracking with Shake-The-Box (Schanz et al. 2016) and data assimilation techniques, like FlowFit (Gesemann et al. 2016) or VIC+ resp. VIC# (Schneiders and Scarano2016, Jeon 2021), raise hope that for moderate Reynolds numbers the full (time-resolved) velocity gradient tensor might be captured experimentally at high-spatial resolution more accurately than in previous generic turbulence measurements based e.g. on PTV, Tomo- or scanning stereo PIV. In Schröder et al. (2015) it was already shown that the wall-shear stress and instantaneous friction velocity vectors in a zero-pressure turbulent boundary layer flow at $Re_\theta = 2770$ could be estimated accurately by STB from particle tracks in close vicinity of the wall. In the work presented here, we attempt to increase the spatial range and resolution down to ~η at moderate image magnification by detecting a sufficient number of events with close tetrahedron particle track constellations in order to reach statistical convergence for determining all terms of

the dissipation rate tensor in homogeneous turbulence directly without losing the global picture of the surrounding energy containing flow structures in the inertial range. At the same time, we are reducing the noise level for determining the related instantaneous velocity gradients from such particle constellations by making use of an optimal temporal TrackFit algorithm and of analytical spatial derivatives along 3D 3rd-order B-splines resulting from the FlowFit algorithm (both see Gesemann et al. 2016). Particle position error issues with multi-point statistics in close proximity due to diffraction limited imaging of particles in several camera projections can be reduced (in future investigations) by using functional approaches finding optimal intermediate time instances along involved particle tracks and weighted uncertainty quantifications as proposed by Godbersen and Schröder 2020 and 2021.

Here, we present measurements of the full velocity gradient tensor and all dissipation rate terms based on dense fields of fluid particle trajectories in von Kármán flow turbulence at Re_λ ~270 and ~370 in between two counter-rotating disks with impellers. Applying the Shake-The-Box (STB) particle tracking algorithm (Schanz et al. 2016) we are able to instantaneously track up to ~80,000 particles in a measurement volume of 40 x 40 x 15 mm³, corresponding to approximately (360×360×130) η^3 for Re_λ ~270 and (650×650×240) η^3 for Re_λ ~370. The mean inter-particle distance is lower than 7 Kolmogorov lengths η at the lower Reynolds number and larger than 9 η for the higher Reynolds number case. The data assimilation scheme FlowFit (Gesemann et al. 2016) applies Navier-Stokes- constraints by imposing conservation of mass and momentum to interpolate the scattered Lagrangian velocity and acceleration data by continuous 3D 3rd order B-Splines in a grid of cells, enabling to recover (locally) the smallest flow scales for the time-resolved 3D velocity, acceleration and pressure fields.

2. Experimental set-up and procedure

The experimental setup at the flow facility GTF3 of MPI-DS in Göttingen consists of a cylindrical water tank (D = 480 mm diameter and H = 580 mm height) with two counter-rotating impellers with d = 250 mm diameter and equipped with 8 baffled vanes of height h= 5 cm at the top and at the bottom, generating a von Kármán flow with a homogeneous turbulent region in the center (at least in radial directions). From earlier experiments (Jucha et al. 2014), the expected Kolmogorov length for the lower Re_λ was η ~ 100 μm at an impeller frequency of 0.5 Hz. The corresponding Kolmogorov time was approximated at τ ~ 10 ms, such that a temporal oversampling of τ by a factor of 12.5 at 1.25 kHz frame rate has been realized by the current LPT experiment. Both values are based on the estimation of ε from a velocity/acceleration-structure function approach by Jucha 2014 and are further improved by the current investigation (see Table 1). Spherical monodisperse and nearly neutrally buoyant polystyrene particles *Dynoseeds TS 20* from *Microbeads* (at 20μm

diameter at ρ = 1,05 g/cm³), which corresponds to a Stokes number of approximately 1 ×10^{-4} for Re$_\lambda$ = 270, are illuminated by a fiber-coupled 150 W Nd:YAG high frequency laser (*IB Chronos 400 MM IC* SHG) in the center of the tank. Four CMOS cameras from *Vision Research* (*Phantom v640*, 2560 x 1600 pixel, operated at reduced resolution of 1280 x 1200 pixel and repetition rates of 1,250 Hz (Re_λ~270) and 3,333 Hz (Re_λ~370)) equipped with 100 mm *Zeiss macro* lenses (at f$_\#$ = 16) and Scheimpflug adapters record the light scattered by the particles in symmetric ~45° tetrahedral forward scattering directions. Water-filled glass prisms attached to the tank windows avoid astigmatism of particle images. See photograph and sketch of the set-up at the GTF3 of MPI, Göttingen in Figure 1. Table 1 shows the experimental parameter settings, including new values for ε resulting from the current investigation.

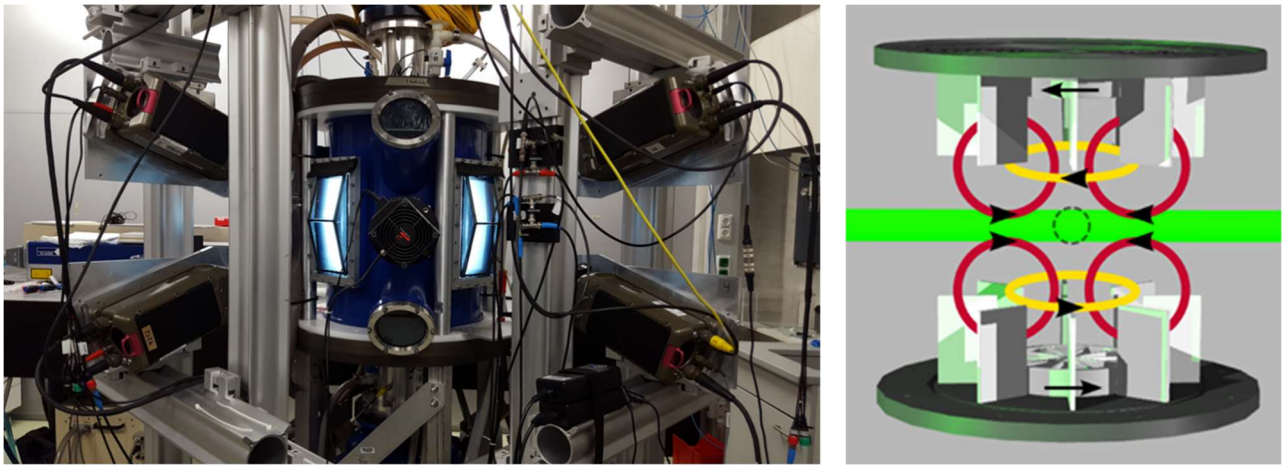

Figure 1: Experimental set up-with four 4 Mpx high speed cameras (v640) for dense Lagrangian Particle Tracking inside the GTF 3 facility at the MPI-DS, Göttingen using Shake-The-Box (left). The turbulent von Kármán flow at Re$_\lambda$ = 270 and 370 is produced with two counter-rotating disks with impellers following the principle sketch (right)

Various time series of snapshots at two different particle image densities were captured corresponding to two different particle concentrations. While the lower seeding density measurements aimed at full convergence of Lagrangian particle statistics, high seeding density measurements were performed for highly resolved Eulerian velocity vector fields and respective velocity gradient tensor and pressure fields statistics. For the former, we captured statistically independent image sequences in short "chunks" of 200 and 40 images each, for the latter we used the full-length temporal resolution with the maximum of 14,000 images per time-series, limited by the camera RAM capacity (see Table 1). Note, that the local position accuracy of the Lagrangian tracks using STB evaluation is better at lower ppp-values than at higher ones, consequently leading to higher accurate velocity and acceleration dynamic ranges (DVR and DAR) (see Scahnz et al. 2016, Sciacchitano et al. 2021).

First, a 3D camera calibration based on a two-sided two-plane target from LaVision, volume-self-calibration (VSC) (Wieneke 2008) and the estimation of the particles Optical Transfer Function (OTF) for each camera and sub-volume (Schanz et al. 2013) have been conducted. Then the STB algorithm (Schanz et al. 2016) with recursive application of the IPR method (Wieneke 2013, Jahn et al. 2021) has been applied on the series of time-resolved images from the four high-speed cameras. A two-pass STB approach was employed, which first tracks forwards in time, then reverses the image order and elongates existing tracks backwards in time, while re-connecting possible track-fragments. The particle tracks (up to ~80,000 per time step and measurement volume for the high seeding cases) have been stored and a temporal filter using 3rd order 1D B-splines has been applied with optimal weighting coefficients derived from the cross-over frequency between signal and noise of the particle tracks-position spectrum (Gesemann et al. 2016). The filtered particles positions and the calculated analytical temporal derivatives, velocity and acceleration, are used as input for the above described FlowFit data assimilation method.
Both, statistical convergence of the mean velocity fields, all Reynolds stresses and acceleration components is achieved with statistically independent measurements and the full spatial and temporal development of flow structures for several integral time scales of the inertial subrange is captured.

	Propeller 0.5 Hz	Propeller 1.0 Hz
Flow properties	τ~13.3/12.1ms	τ~?/3.93 ms
	$\eta = 115/110\mu m$	η =?/61.8μm
	Re_λ~270	Re_λ~370
Camera parameters	1280 x 1200 px	1280 x 1200 px
	1.25 kHz (<1/16τ)	3.33 kHz (<1/13τ)
Statistics (lower seeding density)	1000 X 200 imgs	1000 x 200 imgs
	2000 x 40 imgs	2000 x 40 imgs
Spatiotemporal structures (high seeding d.)	37 x 14000 imgs (875τ)	13 x 14000 imgs (1000τ)
Volume	40 x 40 x 15 (11.5) mm³ (360 × 360 × 130) η^3	40 x 40 x 15 (11.5) mm³ (650 × 650 × 240 η^3)

Table 1: Experimental parameter of the STB campaign using two propeller rotation frequencies and related Reynolds numbers of the von Kármán flow facility GTF 3, including recent findings for $\tau;\eta$ based on direct estimation of ε (left of '/' for Re_λ = 270 only) and based on velocity/acceleration-structure function (right of '/' for both Re_λ).

The measurement volume size for the turbulent flow at Re_λ ~ 270, which is the focus of the present investigation regarding the direct estimation of ε (see chapter 4) was ~360 x 360 x 130 η^3, the one for Re_λ ~ 370 was ~650 x 650 x 240 η^3. The cell size of the individual 3D 3rd order B-Splines is chosen to be ~300 µm, corresponding to ~2.7 η for Re_λ = 270 and ~4.8 η for Re_λ = 370 based on findings of the present work. Herewith, a continuous functional representation of the time-resolved velocity (gradient) and pressure fields is given which can be sampled arbitrarily. An example of the gained LPT results by STB and the corresponding Eulerian flow field information from a subsequent application of the FlowFit data assimilation scheme is given in Figure 2. The left image shows dense particle tracks color coded by the u-velocity component, while the right-side image shows the same particle tracks color coded by the x-component of Lagrangian acceleration a_x and iso-surfaces of the Q-value at 2,500 s^{-2} in grey from FlowFit interpolation. The interplay and dynamic formation of vortical structures with different scales in the shear regions between larger bulk flow clusters visualizes nicely the energy transfer and cascade when watching full time-series of the plots shown in Figure 2. The self-organization of flow structures and corresponding pressure fields are guiding Lagrangian tracks through intermittent events of high acceleration and dissipation. For the interpretation of the flow structure dynamics and its embedded Lagrangian fluid elements represented by the LPT data it is important to know that the y-axis is the axial direction of the two counter-rotating impellers and the x-z-directions are the radial directions. The high swirl strength events as indicated by the grey iso-contour surfaces of the Q-value are mainly stemming from secondary instabilities of even larger diameter vortices oriented predominantly in axial direction.

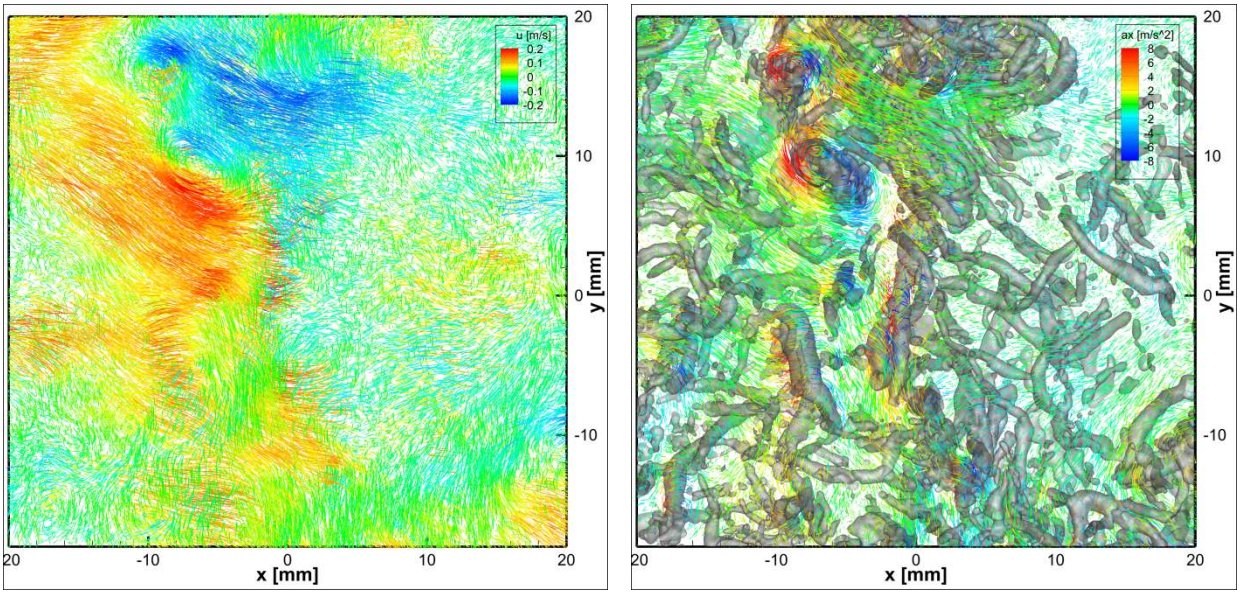

Figure 2: Dense Lagrangian particle tracks measured by STB, color coded by u-velocity (left) and x-component of acceleration and iso-surfaces of Q-criterion, Q= 2,500 s^{-2} from FlowFit (right). Re_λ ~ 270, Von Kármán flow at GTF3 at MPI-DS, Göttingen.

The width of scales captured with temporal-resolution in the present experimental data is covering the full inertial subrange and parts of the dissipative range. The fine-scale resolution of the latter one is depending on the local and average distances of the scattered LPT data in multiples of η given as input for the FlowFit data assimilation. Thus, the smaller dissipative scales of the higher Reynolds number are less resolved (see respective η values in Table 1). For each Reynolds number time resolved image series with in total ~800,000 snapshots in short and long time-series at two different ppp-levels have been acquired and subsequently evaluated by STB and FlowFit, partly with computing resources of the Leibniz HPC SuperMuc in Munich.

3. Global statistics of Eulerian and Lagrangian flow properties

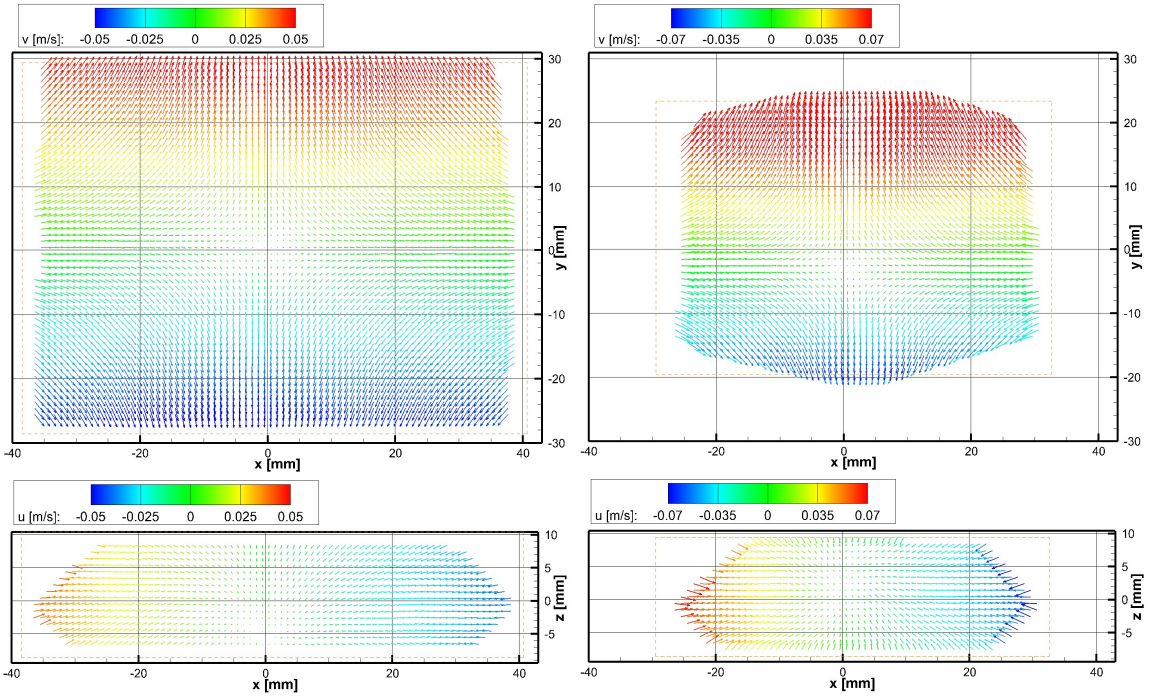

Figure 3: 3D mean velocity vector fields from bin-averaging Lagrangian velocities shown in two central slices of the van Kármán flow measurement volume in x-y- and x-z-directions (y-axial and x- and z- radial components) at 0.5 Hz impeller rotation ($Re_\lambda = 270$) (left) and at 1.0 Hz ($Re_\lambda = 370$) (right). Color coded is the mean axial or y- velocity (top) and the radial or x-velocity (bottom).

In Figure 3 the mean velocity vector fields in two central slices of the GTF3 facility for the two investigated Reynolds numbers provided by a bin-averaging procedure of the Lagrangian velocity vectors over many chunks and time-series are shown. Beside the two differently sized fields-of-view due to a reduced camera resolution at the higher camera frame-rates at $Re_\lambda = 370$ one can see nicely the mean saddle-point structure in the center of the measurement volume with vanishing mean velocity components in all three directions. Even slightly away from the center the mean velocity vectors are relatively small compared to the instantaneous fluctuation velocities (see

Figure 2 (left)). This confirms that the two impellers at the top and bottom of the cylindrical GTF 3 water tank worked synchronously and guaranteed almost homogeneity of the corresponding turbulent dynamics in the central area of the measurement volume. Due to the remaining mean velocity vectors at the outer-most borders of the volume we restricted the field of investigation to 40 x 40 x 15 mm as well for the lower Reynolds number to match the same area for our analysis as for the higher one.

A second indicator for well-defined experimental conditions concerning symmetry and convergence are the PDFs of all three components of Lagrangian accelerations normalized by the respective standard deviations σ_i as shown in Figure 4 for both Reynolds numbers (left and right). The temporal resolution for both cases was $\Delta t \approx \tau/16$ and $\Delta t \approx \tau/13$ allowing for tracking reliably high acceleration events with very limited truncation errors. For the PDFs at $Re_\lambda = 270$ in total $5.3 \cdot 10^9$ and for those at $Re_\lambda = 370$ in total $2.7 \cdot 10^9$ acceleration events have been used for binning enabling a converged statistic down to relatively seldom events with probabilities around $\sim 10^{-6}$. Here, it is remarkable that the standard deviations $\sigma_{x,z}$ for the two radial components are very close to each other, while the ones for the axial-components σ_y are slightly smaller for both flow cases. However, consistent with the literature the higher Reynolds number flow case consists of more intermittent high acceleration events for all components compared to the lower one, while the branches of all PDFs are symmetric for positive and negative signs. The slight slope deviation in the outer branches for the axial components is mainly caused by the lower σ_y values meaning that for high acceleration events the isotropy assumption seems to hold.

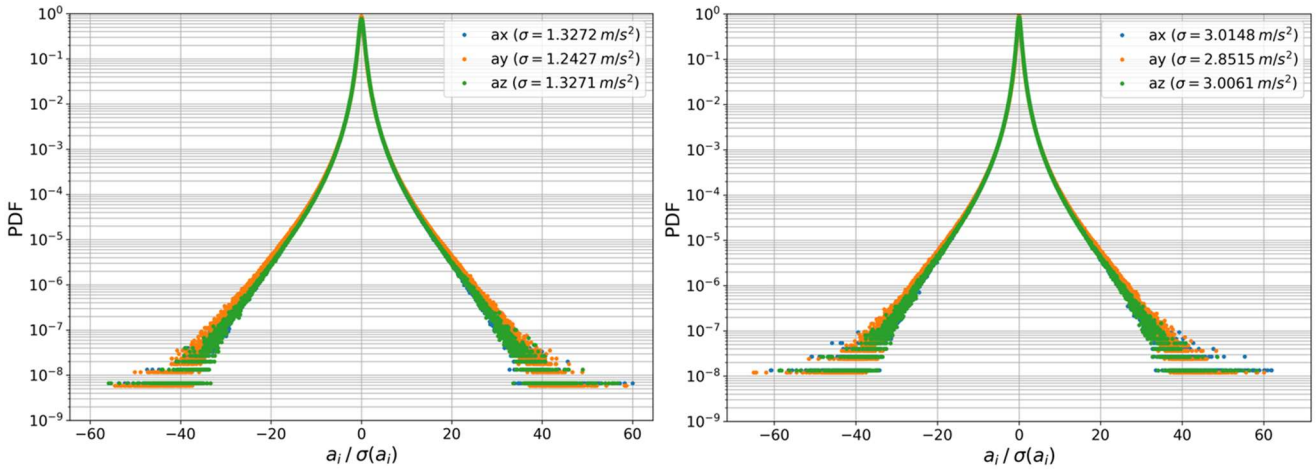

Figure 4: PDFs of Lagrangian acceleration components normalized by the respective standard deviations σ_i at 0.5 Hz impeller rotation frequency ($Re_\lambda = 270$) (left) and at 1.0 Hz ($Re_\lambda = 370$) (right) (both statistics from a central region of the measurement volume).

An interesting (partly) open research topic is the investigation of the Eulerian conditions for high magnitudes of Lagrangian acceleration. We already know from literature that strong vorticity

plays a major role, but as well interactions of Lagrangian tracks with other flow topologies and related strong pressure gradients can create high acceleration events.

4. Results of instantaneous velocity gradients and direct estimations of ε

With the results of FlowFit data assimilation based on dense LPT data from our STB evaluation scheme the full time-resolved velocity gradient tensor and pressure fields are available with a fine-scale resolution depending on the given (mean) 3D particle distances (see above). As can be seen in Figure 5 (top) displaying a simultaneous iso-contour surface representation of the dissipation rate ε at 6.5 x <ε> in grey and of Q-values color coded with u-velocities at Re_λ = 370 the smallest dissipative scales of the flow (e.g. tiny vortex filaments and shear layers) cannot be fully resolved anymore. But still all vorticity structure and dissipation rate dynamics at wave-numbers slightly can be reliably identified especially for events with higher amplitudes. In the shown snapshot it is nicely visible that vortical structures in close interaction are accompanied by high shear flow regions (with similar orientations) which can create large energy dissipation events. These are often elongated parallel and in-between the two or more vortex axes located in close proximity. The time-resolved visualizations of these interplay of ε and Q-values resp. enstrophy ω^2 show many close local dynamic interactions of high swirl- (Q -values) and dissipation structures.

In Figure 5 (bottom-left) the "tear-drop shaped" average Q-R- scatter plot of the invariants of the unconditioned velocity gradient tensor of the corresponding FlowFit results at Re_λ = 370 are shown. Q and R are the invariants of A_{ij} calculated after Chong et al. 1990 with $Q = \frac{1}{2} A_{ij}A_{ji}$ and $R = \frac{1}{3} A_{ij}A_{jk}A_{ki}$,while P = 0 for incompressible flows. The curved discriminant lines in the lower half of the plot separate unstable foci located top-right of the line and stable foci placed top-left of it from unstable nodes below that line on the right-hand side and stable nodes on the left-hand side. Saddle-points are related to the nodes in the other two directions in space and all are located below the discriminant lines in the lower half of the scatter plot.

In Figure 5 (bottom-right) we display the scatter plots of the Q-R- related topologies conditioned by dissipation rate values of ε > 15 x <ε>. We can identify that such high amplitude ε– events are preferably distributed within the nodes and saddle-point regions of the Q-R-plot with a higher location probability along the discriminant boundaries towards unstable foci, where the peak value of this distribution can be found, and towards stable foci. This is consistent with the former observation that high dissipation rate events are organized in shear regions in sheet-like shapes in between vortical motion associated with node-saddle topologies (Elsinga et al. 2017). See as well the work of Buchwald et al. 2022 at the Lisbon Symposium 2022.

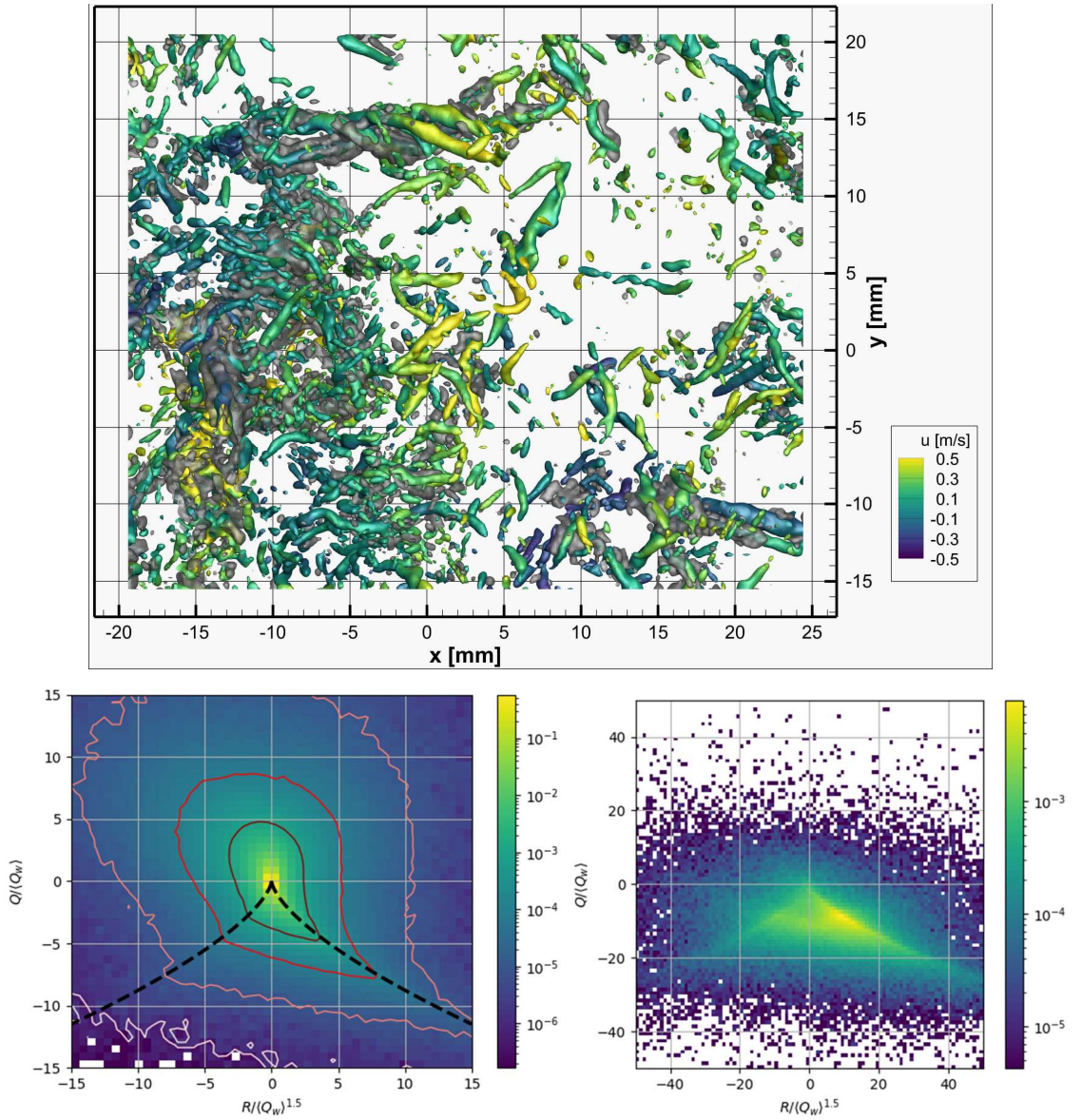

Figure 5: Instantaneous dissipation rate iso-contour surfaces in grey at 6.5 x <ε> and Q-values (7,000 1/s²) color coded by u-velocity (top). Q-R –scatter plot diagrams for all velocity gradient data from A_{ij} (bottom-left) and conditioned for ε > 15 x <ε> (bottom-right) based on FlowFit results at Re_λ = 370. High ε– events are located with higher probability along discriminant boundaries to unstable and stable foci and within area of unstable and stable nodes and saddle-points.

Because of the higher spatial resolution of the measurements and a smaller mean 3D particle distance with respect to η a direct estimation of all terms of ε according to equation (1) using the evaluation scheme with tetrahedrons in close proximity as described above has been processed with approximately one half of the available LPT data at Re_λ = 270 via FlowFit at particles tetrahedron centers. A bin averaging procedure in bins of Δ = 0.5η has collected, averaged and calculated ε from all 12 terms given in equation (1). A curve of the resulting ε value in [m²/s³] in dependence of the average radial distance of the particles around the center of the tetrahedrons is

given by blue dots in Figure 6, left. Furthermore, a PDF distribution of the likelihood of particle tetrahedrons with respect to average radial distances is given in the same figure by an orange curve. The number of entries per bin clearly peaks around 6 η, but due to the high number of volumetric flow field realizations, still millions of entries can be found in the region which form a plateau of ε in bins closer than < 3.5 η radius. The smooth trend towards a plateau on the left-hand side of the graph is a clear indication that we reach resolving the majority of the velocity gradient events contributing to ε, but might as well be a sign of a slight low-pass filtering effect induced by the B-spline grid size or the smoothness constraint (curvature penalization) of the FlowFit scheme. A study on the effect of that FlowFit parameter, which shall guarantee the uniqueness of the solution of the non-linear optimization scheme, will follow a) by investigating the effect of smaller cell sizes for FlowFit data assimilation and b) by determining a precise wave-number spectrum down to the dissipative scales from two-point-correlations based on functional binning (Godbersen et al. 2021). These results shall be presented in a full journal publication.

Averaging the plateau region (red frame in Figure 4) of radial distance bins from 1,5 η to 3.5 η (165 µm to 385 µm) using a total of $9.4 \cdot 10^6$ events leads to a new direct estimation of ε for $Re_\lambda = 270$ based on equation (1) and as many instantaneous entries in the center of the found tetrahedrons:

$$\varepsilon = 0.0057\ m^2/s^3 \rightarrow \eta = \left(\frac{\nu^3}{\varepsilon}\right)^{1/4} = 115.42\ \mu m, \quad \tau_\eta = \left(\frac{\nu}{\varepsilon}\right)^{1/2} = 13.3\ ms$$

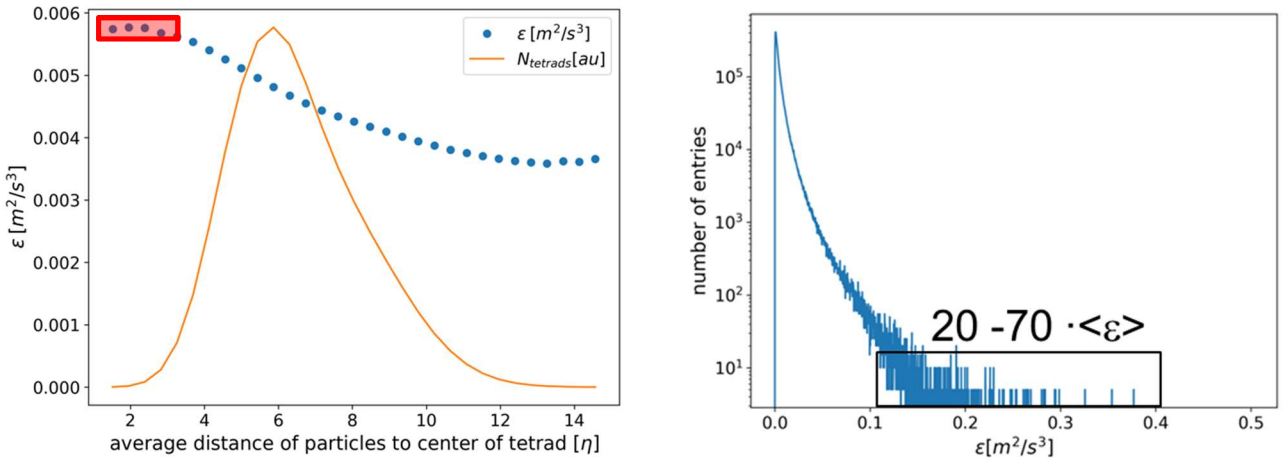

Figure 6: Direct determination of ε by using all 12 terms of the dissipation rate equation. Estimation of instantaneous 3D velocity gradients in the center of tetrahedrons of particles with increasing radial distances in small bins of Δη= 0.5 as given along the x-axis. Average of all entries according to equation (1) for each radial distance bin (blue dots) and probability function of average radial distances of particle tetrahedrons per bin in the STB measurement volume (left). PDF of the ε amplitudes in the investigated sequence of measurement volumes at $Re_\lambda = 270$ in a log-lin plot showing seldom intermittent events with large amplitudes (right).

In bins with average radial distances of particle tetrahedrons smaller than 2 η, not all individual velocity gradient terms of the dissipation rate equation are fully converged due to the smaller number of entries and because they might additionally be affected by the specific choice of the FlowFit's 3rd order B-spline cell size of 300 μm (slight low pass filter effects) and by the remaining position noise of the particle tracks in close proximity. These topics shall be investigated in more detail in an upcoming journal paper. The noise and convergence issues below 2 η are specifically visible for the mixed terms for the equation of ε, while the other entries seem to behave better when reaching closer proximity constellations. However, for most terms and the sum of equation (1) there is a clear trend of reaching a plateau of ε below an average radius of 3.5 η.

In Figure 6, right a PDF of the amplitudes of instantaneous ε events based on the plateau region are shown. The distribution clearly shows very strong intermittent events up to 70 times the mean value of ε. With the existing data set including a quite large range of flow scales it will be possible to link these seldom events to the dynamics of large-scale coherent, or vortical flow structures interacting with each other. Furthermore, we want to show the relation of high ε values with Lagrangian particle accelerations (see Buchwald et al. 2022) looking at Lagrangian tracks passing through such events.

However, the authors are aware that previous DNS results of turbulent flows (Donzis et al 2008) already demonstrated that for large values of dissipation rates ε, which appear often in conjunction with strong enstrophy ω^2 events, one would require a spatial resolution even smaller than η for accurately estimating the respective velocity gradients. An experimental set-up using STB and FlowFit for reaching such high spatial resolutions for the present test case would require approximately a three to four times higher magnification. Such an optical set-up fulfilling the requirement would be easily possible with existing lenses and high-speed cameras, but would require another independent test campaign. However, for the proposed methodology of a direct measurement of all terms of the dissipation rate ε (only) a statistically sufficient number of tetrahedrons of particle tracks in close proximity is required that allows for a local estimation of the velocity gradient tensor down to the smallest scales. Nevertheless, for the individual elements of the velocity gradient tensor a precise Uncertainty Quantification scheme of the whole estimation chain from the LPT results forming the individual tetrahedrons up to the influence of the various FlowFit parameter settings is still pending.

5. Estimation of ε by structure functions in the inertial subrange

The methods estimating ε working on particle trajectories and differences of velocities at two-points with various distances are based on the Kármán-Horwarth equation, extended by Monin and Hill. One, specifically suited for our data, uses the velocity-acceleration structure function (see Falkovich et al. 2012):

$$-2\varepsilon = \langle \delta u \cdot \delta a \rangle \quad (2)$$

to derive the dissipation rate from the averaged differences in velocity and acceleration of neighboring particle pairs in different separations. Another approach applies the second order structure function to derive ε via the relation

$$\langle \delta u_L^2 \rangle = C_2 \cdot (\varepsilon r)^{2/3}, \quad (3)$$

using the averaged longitudinal velocity differences δu_L of particle pairs separated by r. $C_2 \approx 2.1$ is the Kolmogorov constant. Finally, a group of methods uses several varieties of the third order structure function (see e.g. Taylor et al. 2003):

$$\langle \delta u_L^3 \rangle = -4/5 \cdot \varepsilon r, \quad (4)$$

being Kolmogorov's 4/5-law,

$$\langle \delta u_T^2 \delta u_L \rangle = -4/15 \cdot \varepsilon r \quad (5)$$

and

$$\langle \delta u_T^2 \delta u_M \rangle = -4/3 \cdot \varepsilon r. \quad (6)$$

As above, δu_L singnifes the longitudianal velocity difference (being the length of the δu-vector projected onto the separation vector r). δu_T is the transversal velocity difference (being the length of the component of δu perpendicular to r) and δu_M is the magnitude of the velocity difference.
While the methods (3-6), relying on second- and third order structure functions assume homogeneity, isotropy, and a very large (!) Reynolds number, the velocity-acceleration structure function-relation (2) only assumes homogeneity.
The various two-point methods (equations 2-6) were applied to the dataset of Lagrangian particle trajectories in the von Kármán flow gained by STB evaluation for both investigated Re_λ. As the average flow field is vanishing only in the very center of the apparatus (and therefore the measurement domain), the local velocity average was subtracted from the individual particle velocities before calculating the velocity difference (i.e. working on the turbulent fluctuations). The case of $Re_\lambda = 270$ is shown in Figure 7. It can be seen that all methods relying on third-order structure functions (equations 4-6, yellow, green and red curve) are not showing conclusive results over an extensive range of separations. The lack of a clear plateau might be explained by the anisotropic conditions and especially by a not well-developed inertial range at this relatively low Reynolds-number. The shape of the measurement volume is reflected in these curves as a distinctive bump at around 14 mm, which corresponds to the maximum separation of two particles along the z-axis. Relation (3), using the second-order velocity structure function, is

showing a more stable curve between 0.006 m^2/s^3 and 0.008 m^2/s^3, though still a clear plateau is not seen. The velocity-acceleration structure function-relation (2), which assumes only homogeneity, exhibits a nearly stable course from 10 to approx. 45 mm separation, at an average value of around $\varepsilon \approx 0.0069\ m^2/s^3$. This result sits in-between the ones gained by the direct method ($\varepsilon \approx 0.0057\ m^2/s^3$) and the one found in (Jucha 2014b) from experiments at the same apparatus and impeller driving frequency, albeit with a slightly different inner geometry ($\varepsilon \approx 0.0084\ m^2/s^3$) and a lower accuracy for the estimation of velocity and acceleration. A total of 621 x10^9 particle pairs were examined for each method. Figure 7 (right) shows the distribution of separations, with a maximum of approx. 1.5·10^9 entries per 100 μm wide bins.

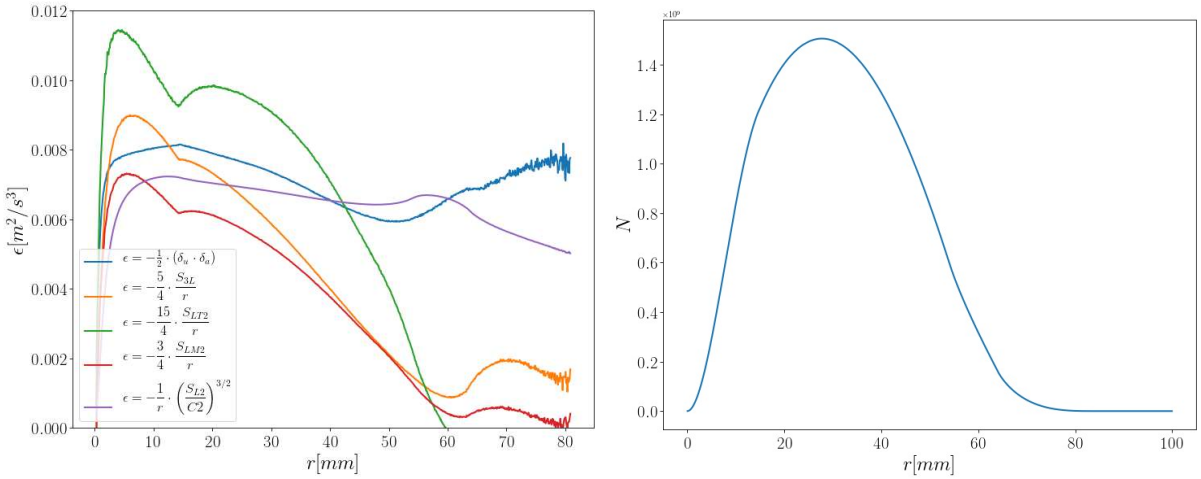

Figure 7: (left) Dissipation rate ε in relation to the separation length r, as given by relations (2-6) for Re_λ = 270; (right) Number of particle pair entries x 10^9 per bin (bin-size = 100 µm).

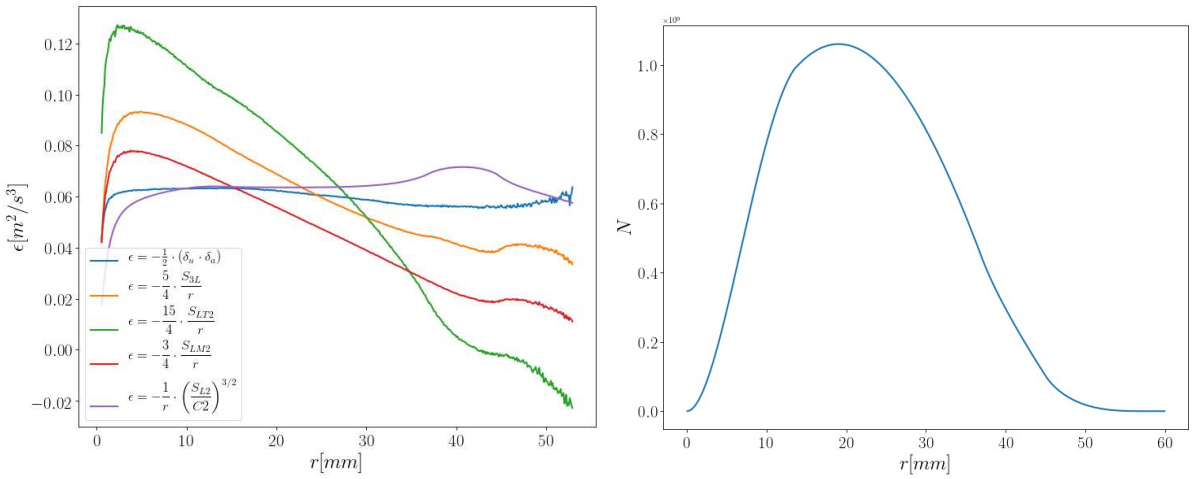

Figure 8: (Left) Dissipation rate ε in relation to the separation length r, as given by relations (2-6) for Re_λ = 370; (Right) Number of particle pair entries x 10^9 per bin (bin-size = 100 µm).

The results for Re_λ = 370, with an impeller frequency of 1 Hz are shown in Figure 8. As in the case with lower Re_λ, the relations (4-6) do not yield a stable plateau. Relations (2) and (3) however both

show a clear plateau from 10 to 30 mm particle distance at the same value of $\varepsilon \approx 0.063\, m^2/s^3$. This value also falls between the ones found in (Jucha 2014b) for $Re_\lambda = 350$ ($\varepsilon \approx 0.053\, m^2/s^3$) and $Re_\lambda = 390$ $\varepsilon \approx (0.09\, m^2/s^3)$. Therefore, we believe the found values to be reliable. Unfortunately, the evaluation using the direct method at the high Re_λ is less converged at the small radial tetrahedron distances below $r < 3\eta$ so that a direct comparison here is even less conclusive.

Concerning the uncertainty of the found values, a thorough investigation has been carried out for method (2) in (Jucha 2014b), which concluded that the number of unknown error sources is too great to allow an analytic derivation. Instead, an empirical uncertainty of 10 % was derived from the noise of the curve. We follow that approach and give the value of 10 % as an upper limit to the uncertainty, as our dataset used more independent measurements, the velocity and acceleration values are believed to be more accurate and the curve therefore exhibits less noise. The same rule is applied to method (3), while methods (4-6) seem not to be applicable due to anisotropy with respect to the radial and axial velocity components and the low Reynolds number.

As seen in the plateaus of Figures 7 and 8, the respective $\langle \delta u \cdot \delta a \rangle$ velocity- acceleration structure function approach leads to the following ε and corresponding η and τ_η values for the lower and higher Reynolds number, respectively:

$\langle \delta u \cdot \delta a \rangle$ approach for $Re_\lambda = 270$: $\varepsilon = 0.0069\, m^2/s^3 \rightarrow \eta = \left(\frac{\nu^3}{\varepsilon}\right)^{\frac{1}{4}} = 110.05\, \mu m, \quad \tau_\eta = \left(\frac{\nu}{\varepsilon}\right)^{\frac{1}{2}} = 12.1\, ms$

$\langle \delta u \cdot \delta a \rangle$ approach for $Re_\lambda = 370$: $\varepsilon = 0.063\, m^2/s^3 \rightarrow \eta = \left(\frac{\nu^3}{\varepsilon}\right)^{1/4} = 61.79\, \mu m, \quad \tau_\eta = \left(\frac{\nu}{\varepsilon}\right)^{1/2} = 3.93\, ms$

The value of ε gained by the $\langle \delta u \cdot \delta a \rangle$ velocity- acceleration structure function for the smaller Reynolds number is slightly higher than the one derived by the newly proposed direct method and thus the values for η and τ_η are slightly lower. The possible reasons for this underestimation of ε (e.g. low-pass-filter effects from still too high particle distances, the B-spline cell size, the curvature penalization and particle position noise) will be investigated further. The smooth plateau of the $\langle \delta u \cdot \delta a \rangle$ velocity- acceleration structure function at the higher Reynolds number gives us a much more reliable estimates for both Reynolds numbers and the comparison with the results of the direct method.

6. Conclusions and Outlook

Several approaches of determining the turbulent dissipation rate ε based on two-point statistics of STB particle trajectories as well as on continuous FlowFit representations of the same were developed and implemented. The latter allows for determining all 12 dissipation rate terms ε, while being free of assumptions, which was newly developed within the scope of the present

work. We showed Lagrangian acceleration statistics, as well as the Eulerian counterparts on velocity and pressure gradients with respective Q-R-diagrams of all A_{ij} entries and those conditioned with high dissipation events. We computed all terms of the energy dissipation rate by the newly proposed direct approach using local velocity gradient information gained by FlowFit at midpoints of particle tetrahedrons in close proximity of a few Kolmogorov lengths for Re_λ = 270 and compare the results to known indirect statistical two-point- approaches from the inertial subrange. An uncertainty quantification scheme in order to judge on the accuracy of our direct measurements of all terms of ε via the proposed method using FlowFit shall be delivered in a future investigation.

Acknowledgements

We acknowledge funding from the European High-Performance Infrastructures in Turbulence (EuHIT) consortium for the DTrack measurement campaign and the support of the staff at MPI-DS in Göttingen. Computer resources for this project have been provided by the Gauss Centre for Supercomputing/Leibniz Supercomputing Centre under grant: pr62zi. The work has been partly funded by the Deutsche Forschungsgemeinschaft (DFG) through Grant No. SCHR 1165/5-1 and -2 as part of the Priority Programme on Turbulent Superstructures (DFG SPP 1881). We acknowledge John Lawson for his cooperation during the set-up of the high-speed laser at the MPI-GTF3 facility.

References

Buchwald, T., Schanz, D., Gesemann, S. & Schröder, A. (2022), Investigation of universal small-scale structures in turbulence using Shake-The-Box Lagrangian Particle Tracking and FlowFit, *Lisbon Symposium 2022*, July 11-14, Lisbon, Portugal

Chong, M.S., Perry, A.E., & Cantwell, B.J. (1990), A general classification of three-dimensional flow fields, Phys. Fluids A 2, 765

Davidson, P.A. (2004), *Turbulence: An Introduction for Scientists and Engineers*. OUP Oxford

Donzis, D.A., Yeung, P.K., & Sreenivasan, K.R. (2008), Dissipation and enstrophy in isotropic turbulence: Resolution effects and scaling in direct numerical simulations. *Phys. Fluids*, 20:045108

Elsinga, G., Ishihara, T., Goudar, M.V., da Silva, C.B., & Hunt, J.C. (2017), The scaling of straining motions in homogeneous isotropic turbulence, J. Fluid Mech, 829, 31-64

Falkovich, G., Xu, H., Pumir, A., Bodenschatz, E., Biferale, L., Boffetta, G., Lanotte, A. S. & Toschi, F. (2012), On Lagrangian single-particle statistics. *Phys. Fluids* 24, 055102

Gesemann, S., Huhn, F., Schanz, D., & Schröder, A. (2016), From Noisy Particle Tracks to Velocity, Acceleration and Pressure Fields using B-splines and Penalties, 18th Lisbon Symposium, Portugal
Godbersen, P., & Schröder, A. (2020), Functional binning: improving convergence of Eulerian statistics from Lagrangian particle tracking, Measurement Science and Technology, 31, 9, 095304, IOP Publishing
Godbersen, P., & Schröder, A. (2021), Enhanced functional binning for one-and two-point statistics using a posteriori Uncertainty Quantification of LPT data. Proc. of 14th Intern Symp on PIV 21, Chicago, USA.
Hamlingon, P.E., Schumacher, J. & Dahm, W.J.A (2008), Direct assessment of vorticity alignment with local and nonlocal strain rates in turbulent flows, Physics of Fluids 20, 111703, https://doi.org/10.1063/1.3021055
Jahn, T., Schanz, D. & Schröder, A. (2021), Advanced Iterative Particle Reconstruction for Lagrangian Particle Tracking, Experiments in Fluids 62 (8), 1-24, https://doi.org/10.1007/s00348-021-03276-7
Jeon, Y.J. (2021), Eulerian time-marching in Vortex-In-Cell (VIC) method: reconstruction of multiple time-steps from a single vorticity volume and time-resolved boundary condition. Proc. of 14th Intern Symp on PIV 21, Chicago, USA.
Jucha, J. (2014), Time-Symmetry Breaking in Turbulent Multi-Particle Dispersion, Dissertation, Georg-August-Universität, Göttingen, http://hdl.handle.net/11858/00-1735-0000-0023-98F1-4
Jucha J, Xu H, Pumir A, & Bodenschatz E (2014b), Time-reversal-symmetry breaking in Turbulence, Phys. Rev. Lett. 113, 054501.
Knutsen, A., Baj, P., Lawson, J., Bodenschatz, E., Dawson, J.R., & Worth, N. (2019), The inter-scale energy budget in a von Kármán mixing flow, Preprint under consideration for publication in Journal of Fluid Mech.
Kolmogorov, A.N. (1941), Dissipation of energy in locally isotropic turbulence, *Dokl. Akad. Nauk SSSR* 32(1). English translation in *Proc. R. Soc. Lond. A* (1991) 434, 15–17
La Porta, A., Voth, G.A., Crawford, A.M., Alexander, J., & Bodenschatz E (2001), Fluid particle accelerations in fully developed turbulence, Nature 409, 1017-1019.
Lawson, J.M., Dawson, J.R. (2015), On velocity gradient dynamics and turbulent structure, Journal of Fluid Mechanics 780, 60-98
Malik, N., Dracos, T., & Papantoniou, D. (1993), Particle Tracking in three dimensional turbulent flows – Part II: Particle tracking. Exp Fluids 15:279-294
Ouellette, N.T., Xu, H., & Bodenschatz, E. (2006), A quantitative study of three-dimensional Lagrangian particle tracking algorithms. Exp Fluids 40(2):301-313
Pope, S.B. (2000), Turbulent Flows. Cambridge University Press
Raffel, M., Willert, C., Scarano, F., Kähler, C.J., Wereley, S.T., & Kompenhans, J. (2018), Particle image velocimetry: a practical guide, 3rd edition, Exp Fluid Mech, Springer, Berlin

Saarenrinne, P., & Piirto, M. (2000), Turbulent kinetic energy dissipation rate estimation from PIV velocity vector fields, Exp Fluids 29:300–307
Schanz, D., Gesemann, S., & Schröder, A. (2016), Shake-The-Box: Lagrangian particle tracking at high particle image densities, Exp. Fluids 57:70
Schanz, D., Gesemann, S., Schröder, A., Wieneke, B., & Novara M (2013), Non-uniform optical transfer function in particle imaging: calibration and application to tomographic reconstruction, Meas Sci Technol 24, 024009
Schneiders, J.F.G., & Scarano, F. (2016), Dense velocity reconstruction from tomographic PTV with material derivatives. Exp Fluids 57:139.
Schröder, A., Schanz, D., Gesemann, S., & Willert, C. (2015), Near-wall turbulence characterization using 4D-PTV Shake-The-Box, 11th International Symposium on Particle Image Velocimetry - PIV2015, 14. - 16. Sept. 2015, Santa Barbara, CA, USA
Sciacchitano, A., Leclaire, B., Schröder, A. (2021), Main results of the first Lagrangian particle tracking challenge. 14th Intern Symp on PIV 21, Chicago, USA. https://doi.org/10.18409/ispiv.v1i1.197
Tanaka, T., & Eaton, J.K. (2007), A correction method for measuring turbulence kinetic energy dissipation rate by PIV, Exp. Fluids 42: 893–902
Taylor, M.A., Kurien, S., & Eyink, G.L. (2003), Recovering isotropic statistics in turbulence simulations: The Kolmogorov 4/5th law, Phys. Rev. E 68, 026310
Tokgoz, S., Elsinga, G.E., Delfos, R., & Westerweel, J. (2012), Spatial resolution and dissipation rate estimation in Taylor–Couette flow for tomographic PIV, Exp. Fluids 53 (3),561–583
Toschi, F., & Bodenschatz, E. (2009), Lagrangian Properties of Particles in Turbulence, Annu. Rev. Fluid Mech. 2009. 41:375–404, Doi: 10.1146/annurev.fluid.010908.165210
Vassilicos, J.C. (2015), Dissipation in Turbulent Flows, Annu Rev Fluid Mech 47:95-117
Wieneke, B. (2008), Volume self-calibration for 3D particle image velocimetry, Exp. Fluids 45:549–556
Wieneke, B. (2013), Iterative reconstruction of volumetric particle distribution, Meas. Sci. Technol 24, 024008
Xu, D., & Chen, J. (2013), Accurate estimate of turbulent dissipation rate using PIV data, Exp. Therm. Fluid Sci. 44, 662-672
Xu, H., Pumir, A., & Bodenschatz, E. (2011), The pirouette effect in turbulent flows, Nature Physics 7, 709-712.